



Dominant Patterns of Summer Ozone Pollution in Eastern China and Associated Atmospheric Circulations

Zhicong Yin^{1,2}, Bufan Cao¹, Huijun Wang^{1,2}

¹Key Laboratory of Meteorological Disaster, Ministry of Education / Joint International Research Laboratory of Climate and Environment Change (ILCEC) / Collaborative Innovation Center on Forecast and Evaluation of Meteorological Disasters (CIC-FEMD), Nanjing University of Information Science & Technology, Nanjing 210044, China

²Nansen-Zhu International Research Centre, Institute of Atmospheric Physics, Chinese Academy of Sciences, Beijing, China

Correspondence to: Zhicong Yin(yinzhc@163.com)

Abstract. Surface ozone, a man-made air pollutant, has been severe during summers in the eastern parts of China, damaging human's health and flora and fauna. During 2015–2018, ground-level ozone pollution increased year by year and intensified from south to north. In North China and Huanghuai region, the O₃ concentrations were highest. Two dominant patterns of summer ozone pollution were determined, i.e., a south-north covariant pattern and a south-north differential pattern. The anomalous atmospheric circulations composited for the first pattern manifested as a zonally enhanced East Asia deep trough and as a west Pacific subtropical high whose western ridge point shifted northward. The local hot, dry air and intense solar radiation enhanced the photochemical reactions to elevate the O₃ pollution levels in North China and Huanghuai region. For the second pattern, the broad positive geopotential height anomalies at high latitudes significantly weakened cold air activity, and those extending to North China resulted in locally high temperature near the surface. In a different manner, the west Pacific subtropical high transported sufficient water vapor to the Yangtze River Delta and resulted in locally adverse environment for the formation of surface ozone. Furthermore, the implications for the interannual differences in summer O₃ pollution have also proven to be meaningful.

1. Introduction

Ozone occurs both in the stratosphere and at ground level. Stratospheric ozone forms a protective layer that shields us from the sun's harmful ultraviolet radiation. However, surface ozone is a man-made air pollutant and has harmful effects on people and on the environment, such as damaging human lungs (Day et al., 2017) and destroying agricultural crops and forest vegetation (Yue et al., 2017). Worldwide, severe ozone events are more frequent and stronger in China than those that have taken place in Japan, South Korea, Europe, and the United States (Lu et al. 2018). Due to their close relationship with anthropogenic emissions (Li et al., 2018), the high O₃ concentrations in China are mainly observed in urban regions, such as in North China (NC), the Yangtze River Delta (YRD) and the Pearl River Delta (PRD) where rapid development has occurred in recent decades (Wang et al., 2017). An increase in surface ozone levels was found in China in 2016 and 2017 relative to 2013 and 2014 (Lu et al., 2018). The O₃ pollution levels in Beijing-Tianjin-Hebei (part of NC) were the most severe in China (Wang et



al., 2006; Shi et al., 2015) and this situation has been getting worse. The O₃ concentrations in North China underwent a significant increase in the period of 2005–2015, with an average rate of 1.13±0.01 ppb yr⁻¹ (Ma et al., 2016). Even on the highest mountain over NC, Mount Tai, summer (June-July-August, JJA) O₃ increased significantly by 2.1ppbv yr⁻¹ (Sun et al., 2016). The O₃ levels generally presented increasing trends from 2012 to 2015 in the YRD (Tong et al., 2017), e.g., the O₃ concentrations in Shanghai (a mega-city) increased by 67% from 2006 to 2015 (Gao et al., 2017). In the PRD region, O₃ increased by 0.86 ppbv yr⁻¹ from 2006 to 2011 (Li et al., 2014). Severe ozone pollution is projected to increase in the future over eastern China (Wang et al., 2013).

Although deep stratospheric intrusions may elevate surface ozone levels (Lin et al., 2015), the main source of surface ozone is the photochemical reactions between the oxides of nitrogen (NO_x) and volatile organic compounds (VOC), i.e., NO_x + VOC = O₃. The concentrations of NO_x and VOC are fundamental drivers impacting ozone production, and are sensitive to the regime of ozone formation, i.e., NO_x-limited or VOC-limited (Jin and Holloway 2015). The changes in fine particulate matter are also a pervasive factor for the variation in ozone concentration. Li et al (2018) found that rapid decreases in fine particulate matter levels significantly stimulated ozone production in NC. Furthermore, the meteorological conditions also influenced the ozone levels via modulation of the photochemical episodes (Yin et al., 2019). Violent solar radiation accelerated chemical O₃ production (Tong et al., 2017). A severe heat wave in the YRD contributed to high O₃ concentrations in 2013 (Pu et al., 2017). Winds had an impact on the O₃ and its precursors at downwind locations (Doherty et al., 2013). Local meteorological influences are always related to specific large-scale atmospheric circulations. The changes in the East Asian summer monsoon led to 2–5% interannual variations in surface O₃ concentrations over central eastern China (Yang et al., 2014). Continental anticyclones created sunny and calm weather, which are favourable conditions for O₃ production in NC (Ding et al., 2013; Yin et al., 2019). Due to their large-scale descending motion, tropical cyclones are often related to the evaluation of surface O₃ levels in the PRD (Ding et al., 2004). Further studies showed that a strong west Pacific subtropical high (WPSH) was unfavourable for the formation of O₃ in South China, due to the association with more clouds, more rainfall, decreased ultraviolet radiation and lower air temperatures (Zhao and Wang, 2017).

Wang et al (2017) reviewed the meteorological influences on ozone events, but the referenced findings were published mainly before 2010, when measurements in China were still scarce. Since 2015, O₃ measurements in eastern China were steadily and widely implemented, but the O₃-weather studies mainly focused on several synoptic processes. Nevertheless, the dominant patterns of summer ozone in east of China are still unclear, which is the topic of this study. The findings of this study basically help to understand the features of surface ozone pollution in eastern China, their relationships with large-scale atmospheric circulations and the implications for the climate variability.



60 2. Data sets

Public hourly O₃ concentration data since May 2014 are available on the website (<http://beijingair.sinaapp.com/>). Although the summer data from 2014 can be downloaded, the observations of atmospheric compositions were beginning to be uniformly distributed and continuously achieved in eastern China since 2015. After processing missing values, 868 sites in eastern China (110°E–127°E, 22°N–45°N) from 2015 to 2018 were employed here to reveal the features of surface ozone pollution and its associated mechanisms. The maximum daily average 8 h concentration of ozone (MDA8) is the maximum of the running 8 h mean O₃ concentration during an entire 24 hour day. According to the Technical Regulation on Ambient Air Quality Index of China (the Ministry of Environmental Protection of China, 2012), MDA8 is generally used to represent the O₃ conditions.

The 2.5°×2.5° ERA-Interim data used here include the geopotential height (Z), zonal and meridional wind, relative humidity, vertical velocity, air temperature at different pressure levels, surface air temperature (SAT) and wind, downward solar radiation at the surface, low and medium cloud cover and precipitation (Dee et al. 2011). Because the maximum photochemical activity often occurred at afternoon (Wang et al., 2010), the daytime data (i.e., 08 a.m.–08 p.m. Beijing time) were calculated by the sub-daily reanalysis to composite the daytime atmospheric circulations and daytime meteorological conditions. In addition, the monthly ERA-Interim reanalysis was also employed here to discuss the impacts of atmospheric circulations on interannual differences or the climate variability of O₃ pollutions in eastern China.

75 3. Variations and dominant patterns

During 2015–2018, summer surface ozone pollution was severe in China, especially in the economically developed regions. Spatially, the JJA mean MDA8 increased from south to north in eastern China (Figure 1a). To the south of 28°N (i.e., South China), the mean MDA8 was mostly lower than 100 µg/m³ and the ozone pollution was obviously lower than that in North China and in the Huanghuai area (NH). It is notable that MDA8 in the PRD was relatively higher than that for the surrounding areas. The mean MDA8 was above 130 µg/m³ to the north of 32°N (i.e., the NH area), and thereinto, the large values of MDA8 centred on the Beijing-Tianjin-Hebei region and in western Shandong province exceeded 150 µg/m³. In the transitional zone, i.e., between 28°N and 32°N, the MDA8 varied from 100 µg/m³ to 120 µg/m³. Surface O₃ pollution was closely linked to the anthropogenic emissions that dispersed and concentrated in the large cities. In the YRD and PRD, high levels of MDA8 were around the large cities. However, the high-level O₃ values in the NH region were contiguous, indicating extensively severe surface O₃ pollution.

The maximum values of MDA8 for four summers were extracted to evaluate the levels of O₃ pollution from another angle (Figure 1b). To the north of 30°N, the maximum MDA8 at most sites was above 265 µg/m³, indicating that the levels of O₃ pollution had exceeded the threshold of severe surface O₃ pollution in China (The Ministry of Environmental Protection of China, 2012). In Beijing and Tianjin, two large cities in NC, the MDA8 values were nearly above 100 µg/m³ and frequently



90 exceeded $215 \mu\text{g}/\text{m}^3$ (Figure 2a). The percentage of non- O_3 -polluted days ($<100 \mu\text{g}/\text{m}^3$) and moderate O_3 -polluted days (>215
 $\mu\text{g}/\text{m}^3$) were 14.4% and 15.3%, respectively, indicating that more than 85% O_3 concentrations exceeded the health threshold
and that for more than 15% of summer days, O_3 concentrations moderately damaged human health. The maximum MDA8 in
the north of Hebei province and in eastern Shandong province even exceeded $320 \mu\text{g}/\text{m}^3$, which badly injured the health of
local citizens. In Shijiazhuang and Weifang, the MDA8 levels were lower than those in Beijing and Tianjin during 2015–2016,
95 but dramatically increased to levels comparable to those of Beijing and Tianjin in 2017 and 2018 (Figure 2b). In Nanjing and
Shanghai, located in the YRD, the MDA8 did not show a clear increasing trend (Figure 2c). Similar to the distribution of the
mean MDA8, the maximum MDA8 to the south of 30°N was lower by comparison. Although approximately 60% of summer
days were non- O_3 -polluted in the cities of Guangzhou and Zhongshan (Figure 2d), severe O_3 pollution also occurred in the
PRD (Figure 1b). The surface O_3 levels in Fujian province were the lowest seen in eastern China, represented by both the mean
100 MDA8 of $70\text{--}90 \mu\text{g}/\text{m}^3$ and maximum MDA8 of $160\text{--}200 \mu\text{g}/\text{m}^3$. These features, i.e., high-level MDA8 and south-north
differences, can also be observed in the MDA8 measurements for each year (Figure S1).

For the ten representative stations with severe ozone pollution, the daily variations in MDA8 were evident (Figure 2–3),
indicating large influences by the daily meteorological variables. Generally, the peak in the summer surface ozone
concentrations occurred in June in the northeast China, and then decreased in July–August due to abundant rainfall in Beijing
105 (Ma et al., 2016). Except for 2015, monthly MDA8 peaked in June and then declined in July and August for the sites to the
north of 30°N , i.e., in Beijing, Tianjin, Tangshan, Taiyuan, Weifang, Shijiazhuang (Figure 3a–b). However, similar monthly
peaks were not obvious for the cities to the north of 30°N (Figure 3c–d).

Considering the characteristics of the observed MDA8 mentioned above, an empirical orthogonal function (EOF) was used to
explore the dominant patterns of summer ozone pollution in eastern China (Figure 4). The percentage of variance contribution
110 for the first three patterns were 21.5%, 15.5% and 8% respectively. Approximately 37% of the variability in the original data
was contained in the first two patterns, therefore, they were defined as the dominant patterns of surface ozone pollution. In the
first EOF pattern (PAT1), the observed MDA8 at different sites changed similarly and the centre of variation was located in the
NH area (Figure 4a). The time series of EOF1 showed that the ozone pollution during 2017–2018 was more serious than that in
2015 and 2016 (Figure 4b). Differently, the second EOF pattern (PAT2), showed notable south-north difference, with centres
115 in the NC and YRD regions (Figure 4c). The time coefficient of PAT2 also did not show an obvious increasing trend (Figure
4d). The PAT1P (PAT2P) and PAT1N (PAT2N) events were defined as when the time series of EOF1 and EOF2 were greater
than one standard deviation and less than $-1 \times$ one standard deviation, respectively. Figure 4 illustrates the composite results
for the dominant patterns of surface ozone. The ozone concentrations for the PAT1P classification were generally greater than
those for PAT1N (Figure 5a–b). The MDA8 values in the NH region were $>160 \mu\text{g}/\text{m}^3$ and $<120 \mu\text{g}/\text{m}^3$ for PAT1P and PAT1N,
120 respectively, indicating significant differences. For the second pattern, the PAT2P appeared as a diminishing pattern from the



north to the south, however, there was severe ozone pollution in the YRD under PAT2N conditions. Therefore, the centres of O_3 variation were NH for the PAT1, and NC and the YRD for the PAT2. From the variations in summer MDA8 (Figure 6), the surface O_3 concentrations in these three areas increased from 2015 to 2017 and remained high in 2018 (Figure 6).

4. Associated atmospheric circulations

125 Associated atmospheric circulations were composited for PAT1 (PAT1P minus PAT1N) and PAT2 (PAT2P minus PAT2N). For the first pattern, the most noticeable O_3 -changed region was NH (Figure 4a). The correlation coefficient between the time series of PAT1 and the NH-averaged MDA8 was 0.97 (Table 1). Thus, the effects of the anomalous atmospheric circulations mainly acted on the photochemical reactions near the surface in NH. There were negative Z850 anomalies over the Ural Mountains, indicating a weaker high ridge. Over the broad region from eastern Eurasia to the north Pacific, the anomalous atmospheric circulations were located zonally, i.e., positive Z850 on the subtropical zone, with cyclonic anomalies at the mid to high latitudes and positive anomalies on the polar region (Figure 7a). The East Asia deep trough was enhanced and extended to northeast China and Japan. The intensity of the East Asia deep trough (i.e., the negative area-averaged Z850) positively correlated with the time series of PAT1 (Table 1) with a correlation coefficient of 0.28 (above the 99% confidence level). In accordance with the deep positive height anomalies to the north of Lake Baikal, which also extended southward to the edge of the Tibetan Plateau, cold air activity was transported to the lower latitudes, but did not arrive at the NH region (Figure 7a). Influenced by the enhanced East Asia deep trough, the main body of WPSH shifted southward. The location of WPSH ($Z500_{(125^{\circ}E, 20^{\circ}N)} - Z500_{(125^{\circ}E, 30^{\circ}N)}$) also showed a positive correlation with the time series of PAT1 ($R=0.39$, Table 1). However, the western ridge point of WPSH was northward and westward than normal (being indicated by $Z500_{(110^{\circ}E, 30^{\circ}N)}$), and occupied the NH area, which was significant with the time series of PAT1 ($R=0.24$, above the 99% confidence level). 140 Although the local anomalous anticyclone over the east of China seemingly delivered water vapor to North China (Figure 7b), the channel of moisture was already cut off in the ocean at low latitudes by the positive and zonal anomalies in the subtropical regions (Figure 7a) and resulted in a dry environment in NH from surface to 500 hPa (Figure 7c). Furthermore, the associated descending motions not only enhanced the efficient adiabatic heating (Figure 7c), but also suppressed the development of convective activity (Figure 7d). The correlation coefficients between the time series of PAT1 and NH-averaged precipitation, SAT, and downward solar radiation at surface were -0.44 , 0.14 and 0.45 , respectively, all of which exceeded the 99% significance test (Table 1). The large-scale atmospheric circulations led to sunny days with high temperatures near the surface (Figure 7a), less precipitation (Figure 7b), a dry environment (Figure 7c) and intense solar radiation (Figure 7d), which substantially enhanced the generation of ozone in NH.

Large amplitudes of PAT2 O_3 were distributed in the NC and YRD regions, and furthermore, the correlation coefficient 150 between the time series of PAT2 and the MDA8 difference between NC and the YRD was 0.77 (Table 1). The impacts of



atmospheric circulations on the photochemical reactions in the above two areas are analysed in Figure 9. Due to the broad positive Z500 anomalies at the high latitudes of Eurasia, the subjacent surface air temperatures significantly increased, indicating weak cold air activity (Figure 9a). Moreover, there were positive Z500 anomalies from the Chukchi Peninsula to Northeast China. In summer, anomalous anticyclonic circulations at the mid and high latitudes generally led to significantly positive SAT anomalies (Figure 9a). The East Asia deep trough was stronger ($R=0.3$), but was limited to the east of Japan.

Extruded by the East Asia deep trough and cyclonic anomalies from the Siberian plains to the YRD, the WPSH moved southward and exhibited southwest-northeast orientation (Figure 9a). The location of WPSH ($Z500_{(110^{\circ}E, 20^{\circ}N)} - Z500_{(110^{\circ}E, 30^{\circ}N)}$) was positively correlated with the time series of PAT2 ($R=0.32$, Table 1). The southwest-northeast distribution of WPSH aided water vapor transportation to the YRD region (Figure 9b–c). Combined with significant upward air flow (Figure 9c), more clouds formed at the medium and low levels (Figure 9d) and precipitation was enhanced in the YRD region (Figure 9b). A moist-cool environment, weak solar radiation and obvious wet deposition reduced the ozone concentration in the YRD region. On the other hand, sinking motion with efficient adiabatic heating (Figure 9c) and weak cold activity (Figure 9a) from the north both resulted in a temperature increase in NC (Figure 9a). There was divergence of water vapor and less cloud cover over NC, resulting in dry, hot and sunny weather (Figure 9b, d). Under such meteorological conditions, the generation of surface O_3 was accelerated, and thus, higher MDA8 was observed in NC. The differences in precipitation, SAT, and downward solar radiation at the surface between the NC and YRD regions were calculated and their correlation coefficients with the time series of PAT2 were -0.46 , 0.18 and 0.62 , respectively (Table 1). The significant correlations indicated that the differences in meteorological conditions between NC and YRD regions, associated with the aforementioned anomalous atmospheric circulations, largely contributed to O_3 PAT2.

5. Signals for interannual variability

The O_3 pollution in NH became persistently severe over the past four years, reflected in both the O_3 -polluted areas and in the O_3 concentration (Figure 11). In addition, the number of sites with maximum MDA8 $> 265 \mu\text{g}/\text{m}^3$, located in NH and the YRD, also increased year by year. The summer MDA8 in the PRD was not as high as that in NH and the YRD (Figure 1a), but its maximum O_3 concentration exceeded the threshold for severe surface O_3 pollution in China in each year (Figure 11). The observed summer MDA8 in eastern China also presented evident interannual differences (Figure 11). For example, the spatial patterns of MDA8 anomalies were different in each year (Figure S2). Although the relative variance contributions of the spatial coefficients varied, the first two EOF patterns of MDA8 were always PAT1 and PAT2 in different years, indicating that the extracted dominant patterns were reliable and steady. Sorting by the variance contribution, the dominant patterns were PAT2 and PAT1 in 2015 and 2016 (Figure S2a–d), however, they are PAT1 and PAT2 in the two subsequent years (Figure S2e–h). A question raised here is whether the aforementioned composited signals of atmospheric circulations could provide



implications for the climate variability of the summer O₃ pollution in eastern China. In 2016 and 2018, the variance contribution of the first pattern was almost twice that of the second pattern, and thus, these two years were selected as typical years whose varied patterns were clearly separated. The dominant pattern of 2016 was PAT2 (explaining approximately 24% of the variance), while the MDA8 in 2018 changed as PAT1, with nearly 34% variance contributions (Figure 11d). In 2016, the MDA8 values in NC and the YRD were nearly out of phase (Figure 12a), and the correlation coefficient between them was -0.28 (above the 99% confidence level). Differently, this correlation coefficient was 0.43 (Figure 12b), indicating similar change features in 2018 between the MDA8 levels of NC and the YRD.

The MDA8 anomalies in 2016 were negative in NC, but positive in the YRD and PRD (Figure 10b). The interannual anomalies of atmospheric circulations in 2016, with respect to the mean of 2105–2018 (Figure 13), were consistent with the associated atmospheric circulations for PAT2 (Figure 9). There were positive Z500 anomalies over the north Pacific at the mid to high latitudes (Figure 13a). These positive anomalies not only indicated a weaker East Asia deep trough but also induced a shallow trough from the Chukchi Peninsula to Northeast China. Together with the stronger high ridge over the Ural Mountains, the cold air was transported to the mid latitudes, resulting in a lower SAT for North China (Figure 13a). The western segment of the WPSH was stronger and moved northward, which occupied the YRD and south China and brought moist air flows to North China (Figure 13b). Sufficient moisture formed more low to mid-level clouds, causing a decrease in solar radiation reaching the ground in NC (Figure 13d). Associated with the extending WPSH, sinking motions resulted in a hot, dry air mass near the surface in the YRD region (Figure 13b–c). In addition, decreased cloud cover did not effectively reflect solar radiation, which was an essential condition for the enhancement of the photochemical reactions. Therefore, at the interannual time scale, the atmospheric anomalies, similar to those shown in Figure 9, also played important roles on the spatial pattern of MDA8 anomalies. That is, the atmospheric circulations in 2016 accelerated the formation of surface O₃ in the YRD, but weakened the summer O₃ pollution in NC.

The MDA8 anomalies were mostly positive in the east of China in 2018 (Figure 10d). “-+” Z850 anomalies were located over the Ural Mountains and to the north of Lake Baikal and the Aleutian Islands (Figure 12a), which was consistent with the anomalous patterns in Figure 7. The East Asia deep trough shifted northward, and meanwhile, the western ridge point of WPSH also shifted northward, resulting in a higher SAT in the east of China and accelerating the photochemical conversion for elevating the surface ozone concentration. The local anomalous anti-cyclone over the NH and the Japan Sea also existed in the interannual signals, which induced the divergence of water vapor in southeast China (Figure 12b). Due to the lack of moisture, it was difficult for cloud cover to form, and more solar radiation directly reached the ground (Figure 12d). The large-scale atmospheric circulations led to high temperatures near the surface in eastern China, and to a dry and sunny environment in the YRD and South China. Thus, under such weather conditions, positive MDA8 anomalies were observed in 2018. Although the signals of global warming had impacts on the anomalies of atmospheric circulations, the key features could also be found when



the anomalies were viewed with respect to the climate mean during 1979–2018 (Figure S3–S4). In addition, if the variance contributions of the first two EOF patterns were not significantly different, i.e., in 2015 and 2017, the interannual signals of atmospheric circulations also showed integrated characteristics of PAT1 and PAT2 (Figure S5–S6).

215 6. Conclusions and discussions

During the recent four years, ground-level ozone pollution became the major air challenge in the summers in the east of China. The highest O₃ concentrations were observed in North China and in the Huanghuai region, which are located north of 32°N. The O₃-contaminated air occurred for 85% of summer days in Beijing and Tianjin. In the south, the surface O₃ pollution was also severe both in the Yangtze and Pearl River delta regions. Meteorological conditions had significant impacts on the evident
220 daily fluctuation of MDA8, to reveal their detailed relationships, the dominant patterns of summer ozone pollution and associated atmospheric circulations were analysed in this study.

The MDA8 of the first prominent pattern changed synergistically in the east of China, especially in North China and in the Huanghuai region. An enhanced east Asia deep trough and west Pacific subtropical high were zonally distributed and prevented the northward transportation of moisture. The northward-shifted western ridge point of the west Pacific subtropical
225 high accelerated the photochemical reactions via hot-dry air and intense solar radiation. The second pattern of ozone pollution showed remarkable south-north differences. Broad positive geopotential height anomalies at the high latitudes significantly increased the surface air temperature and thus decreased cold air activities. These positive anomalies also extended to North China and resulted in locally warmer air near the surface. On the other hand, the southwest-northeast oriented west Pacific subtropical high transported sufficient water vapor to the Yangtze River Delta. Consequently, a local moist-cool environment,
230 without intense sunlight, reduced the formation of surface ozone.

The interannual differences in summer O₃ pollution were also discussed and the composited signals of atmospheric circulations and weather conditions proved to have meaningful implications for climate variability. Although the simultaneous large-scale atmospheric circulations were diagnosed on an interannual scale, their possible preceding climate drivers, e.g., sea ice, and sea surface temperature, were still unclear. The research related to climate variability has always needed long-term
235 data. To get around the problem of the data time span, Yin et al (2019) developed an ozone weather index using data from 1979 to 2017 and demonstrated the contributions of Arctic sea ice in May to O₃ pollution in North China. In addition, the dominant patterns of ozone concentrations were also decomposed with the observed data from 2015 to 2018. With the increase in O₃ observations, increasingly reliable dominant patterns and more features might be revealed in the future. At present, the fine particulate matter decreased in the summers in eastern China (Li et al. 2018); however ozone production was significantly
240 enhanced. Thus, attentions to surface pollution should be strengthened and the weather-climate component should be taken into account when making decisions for control measures.



Author contribution

ZY and HW designed the research. BC and ZY performed most of the Figures and analysis. ZY prepared the paper with contributions from all co-authors.

245

Competing interests

The authors declare that they have no conflict of interest.

Acknowledgements

250 This research was supported by the National Natural Science Foundation of China (41421004, 91744311 and 41705058) and the funding of the Jiangsu Innovation & Entrepreneurship team.

References

- 255 Day, D. B., Xiang, J. B., Mo, J. H., Li, F., Chung, M., Gong, J. C., Weschler, C. J., Ohman-Strickland, P. A., Sundell, J., Weng, W. G., Zhang, Y. P., and Zhang J.: Association of Ozone Exposure With Cardiorespiratory Pathophysiologic Mechanisms in Healthy Adults. *JAMA Internal Medicine*, 177(9), 1344-1353, doi:10.1001/jamainternmed.2017.2842, 2017.
- Dee, D. P., Uppala, S. M., Simmons, A. J., Berrisford, P., Poli, P., Kobayashi, S., Andrae, U., Balmaseda, M. A., Balsamo, G., Bauer, P., Bechtold, P., and Beljaars, A. C. M.: The ERAInterim reanalysis: configuration and performance of the data
260 assimilation system, *Quarterly Journal of the Royal Meteorological Society*, 137, 553–597, doi:10.1002/qj.828, 2011.
- Ding, A. J., Fu, C. B., Yang, X. Q., Sun, J. N., Zheng, L. F., Xie, Y. N., Herrmann, E., Nie, W., Petäjä T., Kerminen, V. M., and Kulmala, M.: Ozone and fine particle in the western Yangtze River Delta: an overview of 1 yr data at the SORPES station, *Atmospheric Chemistry and Physics*, 13(11), 5813-5830, doi:10.5194/acp-13-5813-2013, 2013.
- Ding, A. J., Wang, T., Zhao, M., Wang, T. J., Li, Z. K.: Simulation of sea-land breezes and a discussion of their implications on
265 the transport of air pollution during a multi-day ozone episode in the Pearl River Delta of China, *Atmospheric Environment*, 38(39):6737-6750, doi:10.5194/acpd-13-2835-2013, 2004.
- Doherty, R. M., Wild, O., Shindell, D. T., Zeng, G., MacKenzie, I. A., Collins, W. J., Fiore, A. M., Stevenson, D. S., Dentener, F. J., Schults, M. G., Hess, P., Derwent, R. G., Keating, T. J.: Impacts of climate change on surface ozone and intercontinental



- ozone pollution: A multi-model study, *Journal of Geophysical Research Atmospheres*, 118(9), 3744–3763,
270 doi:10.1002/jgrd.50266, 2013.
- Gao, W., Tie, X. X., Xu, J. M., Huang, R. J., Mao, X. Q., Zhou, G. Q., Chang, L. Y.: Long-term trend of O₃ in a mega City (Shanghai), China: Characteristics, causes, and interactions with precursors, *Science of the Total Environment*, 603–604, 425–433, doi:10.1016/j.scitotenv.2017.06.099, 2017.
- Jin, X. M., Holloway T., Spatial and temporal variability of ozone sensitivity over China observed from the Ozone Monitoring
275 Instrument, *Journal of Geophysical Research: Atmospheres*, 120, 7229–7246, doi:10.1002/2015JD023250, 2015.
- Li, J. F., Lu, K. D., Lv, W., Li, J., Zhong, L. J., Ou, Y. B., Chen, D. H., Huang, X., Zhang, Y. H.: Fast increasing of surface ozone concentrations in Pearl River Delta characterized by a regional air quality monitoring network during 2006–2011, *Journal of Environmental Sciences*, 26, 23–36, doi:10.1016/S1001-0742(13)60377-0, 2014.
- Li, K., Jacob, D. J., Liao, H., Shen, L., Zhang, Q., Bates, K. H.: Anthropogenic drivers of 2013–2017 trends in summer surface
280 ozone in China, *Proceedings of the National Academy of Sciences of the United States of America*, 116(2), 422–427, doi:10.1073/pnas.1812168116, 2018.
- Lin, M. Y., Fiore, A. M., Horowitz, L. W., Langford, A. O., Oltmans, S. J., Tarasick, D., and Rieder, H. E.: Climate variability modulates western US ozone air quality in spring via deep stratospheric intrusions, *Nature Communications*, 6(1), 7105–7105, doi:10.1038/ncomms8105, 2015.
- 285 Lu, X., Hong, J. Y., Zhang, L., Cooper, O. R., Schultz, M. G., Xu, X. B., Wang, T., Gao, M., Zhao, Y. H., Zhang, Y. H. Severe surface ozone pollution in China: A global perspective, *Environmental Science & Technology Letters*, 5, 487–494, doi:10.1021/acs.estlett.8b00366, 2018.
- Ma, Z. Q., Xu, J., Quan, W. J., Zhang, Z. Y., Lin, W. L., and Xu, X. B.: Significant increase of surface ozone at a rural site, north of eastern China, *Atmospheric Chemistry and Physics*, 16(6), 3969–3977, doi:10.5194/acp-16-3969-2016, 2016.
- 290 Pu, X., Wang, T. J., Huang, X., Melas, D., Zanis, P., Papanastasiou, D. K., Poupkou, A.: Enhanced surface ozone during the heat wave of 2013 in yangtze river delta region, china, *Science of the Total Environment*, 603, 807–816, <https://doi.org/10.1016/j.scitotenv.2017.03.056>, 2017.
- Shi, C. Z., Wang, S. S., Liu, R., Zhou, R., Li, D. H., Wang, W. X., Li, Z. Q., Cheng, T. T., Zhou, B.: A study of aerosol optical properties during ozone pollution episodes in 2013 over Shanghai, China. *Atmospheric Research*, 153, 235–249,
295 doi:10.1016/j.atmosres.2014.09.002, 2015.
- Sun, L., Xue, L. K., Wang, T., Gao, J., Ding, A. J., Cooper, O. R., Lin, M. Y., Xu, P. J., Wang, Z., Wang, X. F., Wen, L., Zhu, Y. H., Chen, T. S., Yang, L. X., Wang, Y., Chen, J. M., and Wang, W. X.: Significant increase of summertime ozone at Mount Tai in Central Eastern China, *Atmospheric Chemistry and Physics*, 16, 10637–10650, doi:10.5194/acp-16-10637-2016, 2016.



The Ministry of Environmental Protection of China: Technical Regulation on Ambient Air Quality Index, China
300 Environmental Science Press, China, 2012

Tong, L., Zhang, H. L., Yu, J., He, M. M., Xu N. B., Zhang, J. J., Qian F. Z., Feng J. Y., and Xiao, H.: Characteristics of surface ozone and nitrogen oxides at urban, suburban and rural sites in Ningbo, China, *Atmospheric Research*, 187: 57–68, <https://doi.org/10.1016/j.atmosres.2016.12.006>, 2017.

Wang, T., Ding, A., Gao, J., Wu, W. S.: Strong ozone production in urban plumes from Beijing, China, *Geophysical Research*
305 *Letters*, 33(21), 320–337, doi:10.1029/2006GL027689, 2006.

Wang, T., Nie, W., Gao, J., Xue, L. K.: Air quality during the 2008 Beijing Olympics: secondary pollutants and regional impact. *Atmospheric Chemistry and Physics*, 10(16), 7603–7615, doi:10.5194/acp-10-7603-2010, 2010.

Wang, T., Xue, L. K., Brimblecombe, P., Lam, Y. F., Li, L., Zhang, L.: Ozone pollution in China: A review of concentrations, meteorological influences, chemical precursors, and effects, *Science of The Total Environment*, 575, 1582–1596,
310 doi:10.1016/j.scitotenv.2016.10.081, 2017.

Wang, Y. X., Shen, L. L., Wu, S. L., Mickleby, L., He, J. W., and Hao, J. M.: Sensitivity of surface ozone over China to 2000–2050 global changes of climate and emissions, *Atmospheric Environment*, 75, 372–382, doi:10.1016/j.atmosenv.2013.04.045, 2013.

Yang, Y., Liao, H., Li, J. P.: Impacts of the East Asian summer monsoon on interannual variations of summertime
315 surface-layer ozone concentrations over China. *Atmospheric Chemistry and Physics*, 14:6867–6879, doi:10.5194/acp-14-6867-2014, 2014.

Yin, Z. C., Wang, H. J., Li, Y. Y., Ma, X. H., Zhang, X. Y.: Links of Climate Variability among Arctic sea ice, Eurasia teleconnection pattern and summer surface ozone pollution in North China, *Atmospheric Chemistry and Physics*, 19, 3857–3871, <https://doi.org/10.5194/acp-19-3857-2019>, 2019.

Yue X, Unger, N., Harper, K., Xia, X. G., Liao, H., Zhu, T., Xiao J. F., Feng, Z. Z., and Li, J.: Ozone and haze pollution weakens net primary productivity in China, *Atmospheric Chemistry and Physics*, 17:6073–6089, doi:10.5194/acp-2016-1025, 2017.

Zhao, Z. J., Wang, Y. X.: Influence of the west pacific subtropical high on surface ozone daily variability in summertime over eastern china, *Atmospheric Environment*, 170, 197–204, <https://doi.org/10.1016/j.atmosenv.2017.09.024>, 2017.

325

Figures captions

Table 1. Correlation coefficients between the time series of PAT1 (PAT2) and the key indices of atmospheric circulations and meteorological conditions. “***” and “**” indicate that the correlation coefficients were above the 99% and 95% confidence level, respectively.



- 330 **Figure 1.** Distribution of the (a) mean values and (b) maximum values of MDA8 in summer from 2015 to 2018. The black dots indicate the locations of the observation sites.
- Figure 2.** Variations in MDA8 of polluted cities from 2015 to 2018, including (a) Beijing, Tianjin and Tangshan; (b) Taiyuan, Weifang and Shijiazhuang; (c) Shanghai and Nanjing; and (d) Zhongshan and Guangzhou.
- Figure 3.** Boxplots of the MDA8 in June, July and August from 2015 to 2018. The polluted cities included (a) Beijing, Tianjin and Tangshan; (b) Taiyuan, Weifang and Shijiazhuang; (c) Shanghai and Nanjing; and (d) Zhongshan and Guangzhou.
- 335 **Figure 4.** The first EOF pattern (PAT1: a, b) and second EOF pattern (PAT2: c, d) of MDA8 in summer from 2015 to 2018, including the spatial pattern (a, c) and the time coefficient (b, d). The black boxes in panels a and c are the selected North China and Huanghuai region (NH), North China (NC) Yangtze River Delta (YRD) and Pearl River Delta (YRD).
- 340 **Figure 5.** Composites of the MDA8 PAT1 (a, b) and PAT2 (c, d) in summer from 2015 to 2018. Panels a and c were composited when the time coefficient of EOF1 and EOF2 was greater than one standard deviation, while panels b and d were when the time coefficient was less than $-1 \times$ one standard deviation.
- Figure 6.** Variations in the area-mean summer MDA8 from 2015 to 2017 for NH, NC, and YRD.
- Figure 7.** Composites of the daytime atmospheric circulations (i.e., PAT1P – PAT1N). (a) Geopotential height at 850 hPa (contours) and surface air temperature (shading), (b) water vapor flux at 850 hPa (arrows) and precipitation (shading), (c) 100°E–120°E mean wind (arrows) and relative humidity (shading), (d) downward solar radiation at the surface (shading) and the sum of low and medium cloud cover (contours). The white dots indicate that the shading was above the 95% confidence level. The purple boxes in panels a, b and d show the NH region, and the black box in panel a indicates the location of the East Asia trough.
- 345 **Figure 8.** Variations in standardized PAT1 time series, NH-area averaged MDA8 and the key indices of atmospheric circulations (a), and the meteorological conditions (b). The calculations of EAT_1 , $WPSH_1$, Pre_1 , SAT_1 and SSR_1 are consistent with those in Table 1.
- Figure 9.** Composites of the daytime atmospheric circulations (i.e., PAT2P – PAT2N). (a) Geopotential height at 500 hPa (contours) and surface air temperature (shading), (b) water vapor flux at 850 hPa (arrows) and precipitation (shading), (c) 100°E–120°E mean wind (arrows) and relative humidity (shading), (d) downward solar radiation at the surface (shading) and the sum of low and medium cloud cover (contours). The white dots indicate that the shading was above the 95% confidence level. The purple boxes in panel a, b and d are the NC and YRD regions, and the black box in panel a indicates the location of the East Asia trough.
- 355 **Figure 10.** Variations in the standardized PAT2 time series, the MDA8 difference between NC and the YRD and the key indices of atmospheric circulations (a), and the meteorological conditions (b). The calculations of EAT_2 , $WPSH_2$, Pre_2 , SAT_2 and SSR_2 are consistent with those in Table 1.
- Figure 11.** Anomalies in the summer mean MDA8 in 2015 (a), 2016 (b), 2017 (c) and 2018(d), relative to the mean during 2015–2018. The black crosses and dots indicate the locations of the observation sites while the black crosses also indicate that the maximum MDA8 was larger than $265 \mu\text{g}/\text{m}^3$.
- 365 **Figure 12.** Variations in the MDA8 of NC (black) and the YRD (blue) in 2016 (a) and 2018 (b).
- Figure 13.** Anomalies of summer mean atmospheric circulations in 2016, with respect to the mean during 2015–2018. (a) Geopotential height at 500 hPa (contours) and surface air temperature (shading), (b) water vapor flux at 850 hPa (arrows) and precipitation (shading), (c) 100°E–120°E mean wind (arrows) and relative humidity (shading), (d) downward solar radiation at the surface (shading) and the sum of low and medium cloud cover (contours). The white dots indicate that the shading was above the 95% confidence level.
- 370 **Figure 14.** Anomalies of summer mean atmospheric circulations in 2018 with respect to the mean during 2015–2018. (a) Geopotential height at 850 hPa (contours) and surface air temperature (shading), (b) water vapor flux at 850 hPa (arrows) and precipitation (shading), (c) 100°E–120°E mean wind (arrows) and relative humidity (shading), (d) downward solar radiation at the surface (shading) and the sum of low and medium cloud cover (contours). The white dots indicate that the shading was above the 95% confidence level.
- 375



Table 1. Correlation coefficients between the time series of PAT1 (PAT2) and the key indices of atmospheric circulations and meteorological conditions. “***” and “**” indicate that the correlation coefficients were above the 99% and 95% confidence level, respectively.

PAT1	MDA8 ₁	EAT ₁	WPSH ₁	Pre ₁	SAT ₁	SSR ₁
	0.97**	0.28**	0.39**	-0.44**	0.14**	0.65**
PAT2	MDA8 ₂	EAT ₂	WPSH ₂	Pre ₂	SAT ₂	SSR ₂
	0.77**	0.30**	0.32**	-0.46**	0.18**	0.62**

MDA8₁ is the NH-area averaged MDA8, while the MDA8₂ is the MDA8 difference between NC and YRD. EAT₁ and EAT₂ indicate the intensity of the East Asia deep trough and were calculated as the mean $-Z850$, shown in the black boxes in Figure 7 and Figure 9, respectively. WPSH₁ ($Z500_{(125^{\circ}E, 20^{\circ}N)} - Z500_{(125^{\circ}E, 30^{\circ}N)}$) and WPSH₂ ($Z500_{(110^{\circ}E, 20^{\circ}N)} - Z500_{(110^{\circ}E, 30^{\circ}N)}$) represents the location of WPSH. Pre₁, SAT₁ and SSR₁ were calculated as the NH-area averaged precipitation, SAT and downward solar radiation at the surface, respectively. Pre₂, SAT₂ and SSR₂ are the differences in the NC- and YRD-area averaged precipitation, SAT and downward solar radiation at the surface, respectively.

390

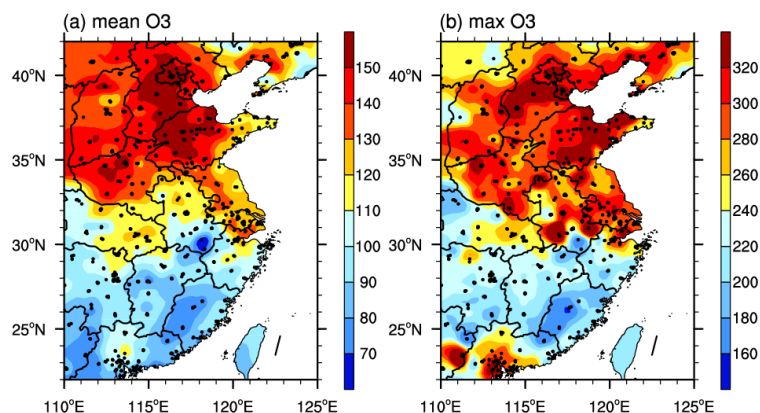


Figure 1. Distribution of the (a) mean values and (b) maximum values of MDA8 in summer from 2015 to 2018. The black dots indicate the locations of the observation sites.

395

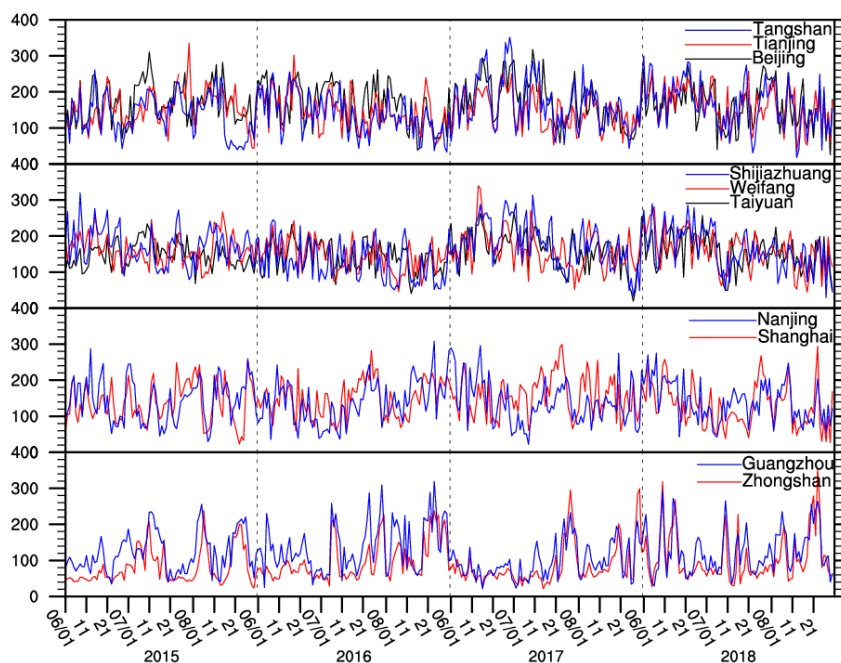
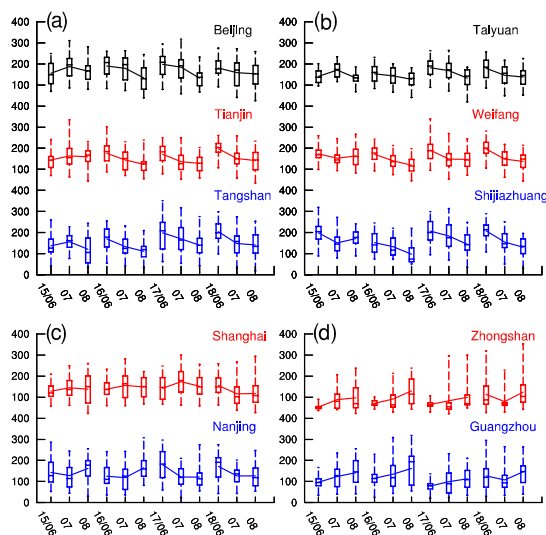
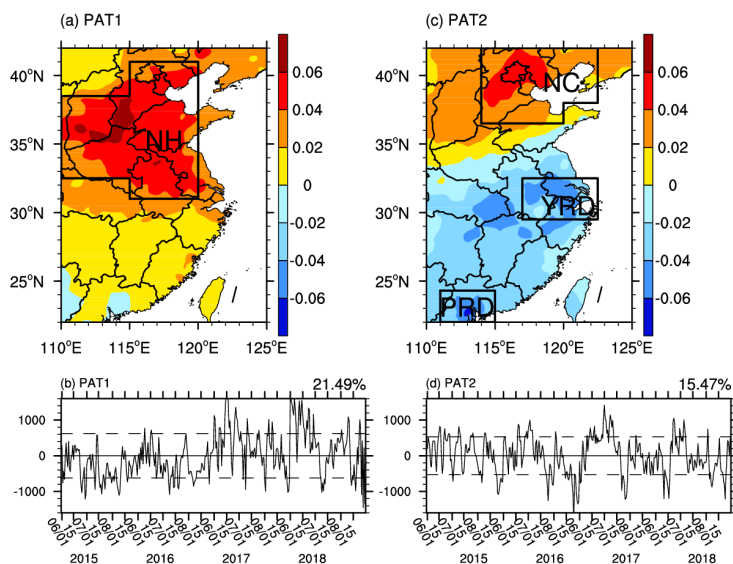


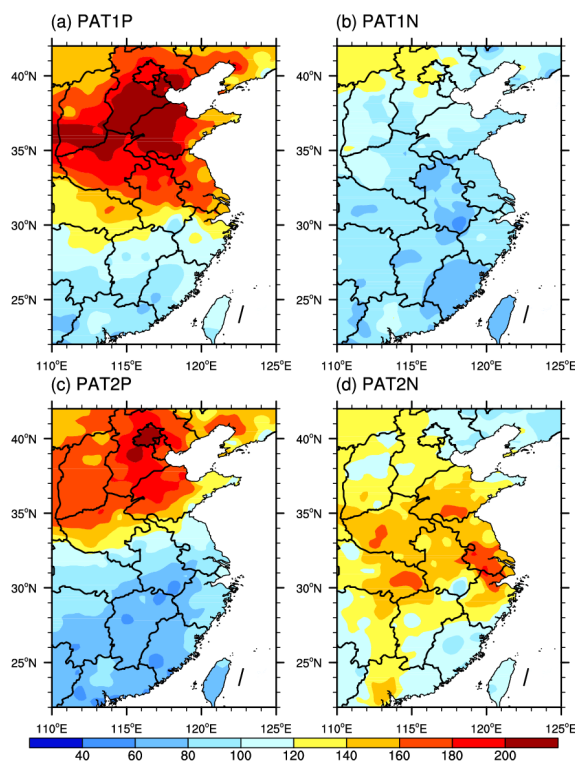
Figure 2. Variations in MDA8 of polluted cities from 2015 to 2018, including (a) Beijing, Tianjin and Tangshan; (b) Taiyuan, Weifang and Shijiazhuang; (c) Shanghai and Nanjing; and (d) Zhongshan and Guangzhou.



400 Figure 3. Boxplots of the MDA8 in June, July and August from 2015 to 2018. The polluted cities included (a) Beijing, Tianjin and Tangshan; (b) Taiyuan, Weifang and Shijiazhuang; (c) Shanghai and Nanjing; and (d) Zhongshan and Guangzhou.



405 **Figure 4.** The first EOF pattern (PAT1: a, b) and second EOF pattern (PAT2: c, d) of MDA8 in summer from 2015 to 2018, including the spatial pattern (a, c) and the time coefficient (b, d). The black boxes in panels a and c are the selected North China and Huanghuai region (NH), North China (NC) Yangtze River Delta (YRD) and Pearl River Delta (YRD).



410 **Figure 5.** Composites of the MDA8 PAT1 (a, b) and PAT2 (c, d) in summer from 2015 to 2018. Panels a and c were composited when the time coefficient of EOF1 and EOF2 was greater than one standard deviation, while panels b and d were when the time coefficient was less than $-1 \times$ one standard deviation.

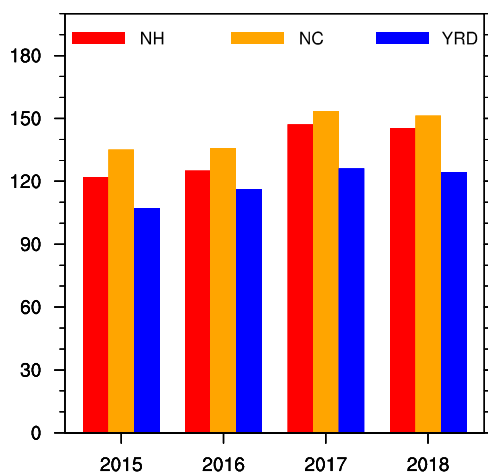
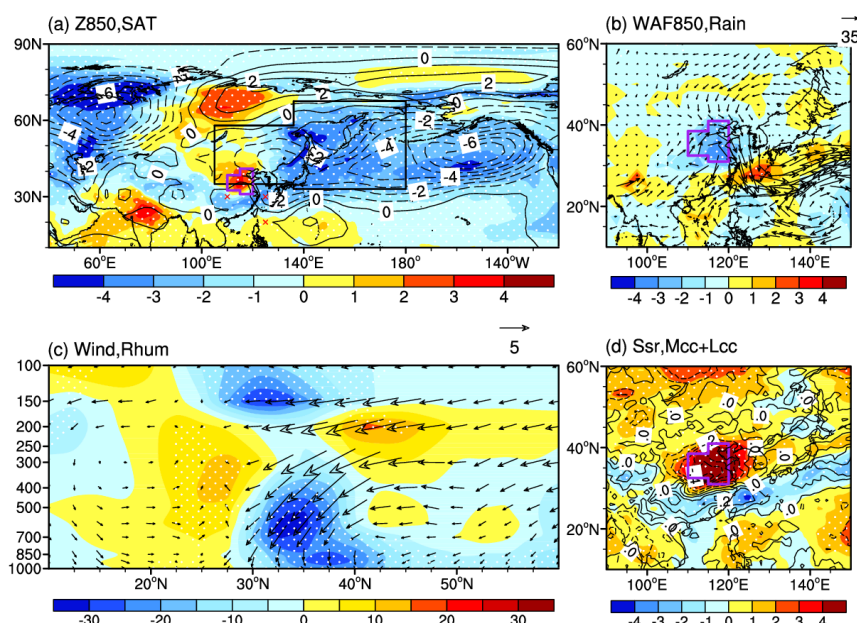


Figure 6. Variations in the area-mean summer MDA8 from 2015 to 2017 for NH, NC, and YRD.

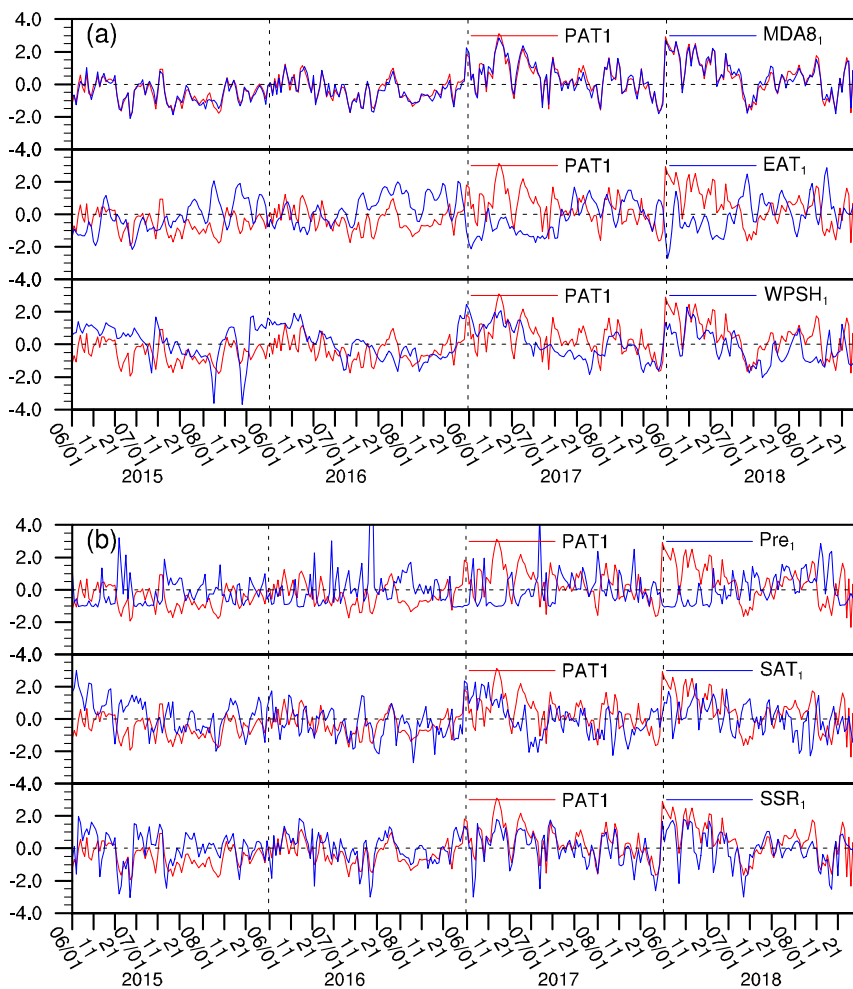


415

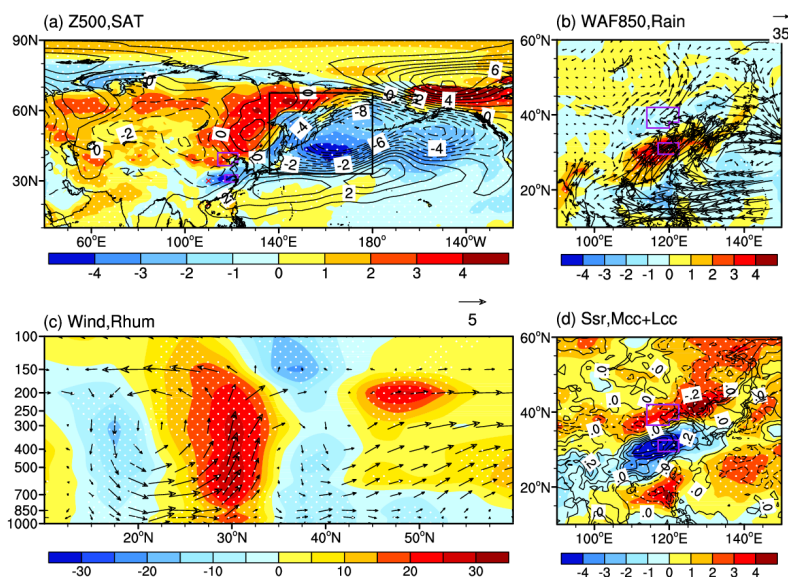
Figure 7. Composites of the daytime atmospheric circulations (i.e., PAT1P - PAT1N). (a) Geopotential height at 850 hPa (contours) and surface air temperature (shading), (b) water vapor flux at 850 hPa (arrows) and precipitation (shading), (c) 100°E–120°E mean wind (arrows) and relative humidity (shading), (d) downward solar radiation at the surface (shading) and the sum of low and medium cloud cover (contours). The white dots indicate that the shading was above the 95% confidence level. The purple boxes in panels a, b and d show the NH region, and the black box in panel a indicates the location of the East Asia trough.

420

425



430 **Figure 8.** Variations in standardized PAT1 time series, NH-area averaged MDA8 and the key indices of atmospheric circulations (a), and the meteorological conditions (b). The calculations of EAT₁, WPSH₁, Pre₁, SAT₁ and SSR₁ are consistent with those in Table 1.



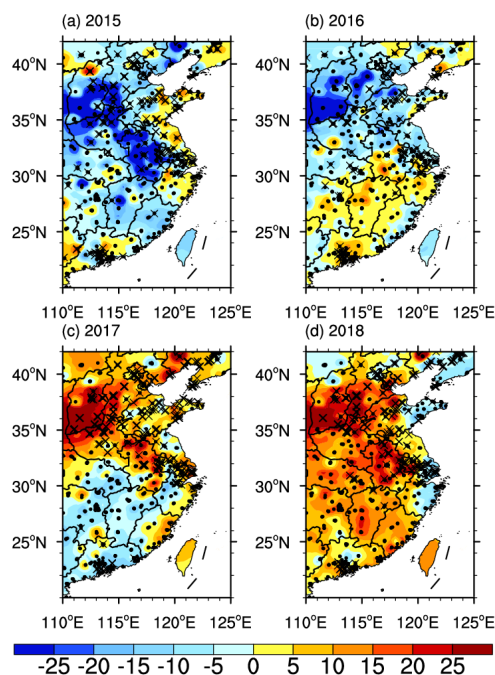
435

440

445

450

Figure 9. Composites of the daytime atmospheric circulations (i.e., PAT2P - PAT2N). (a) Geopotential height at 500 hPa (contours) and surface air temperature (shading), (b) water vapor flux at 850 hPa (arrows) and precipitation flux (shading), (c) 100°E–120°E mean wind (arrows) and relative humidity (shading), (d) downward solar radiation at the surface (shading) and the sum of low and medium cloud cover (contours). The white dots indicate that the shading was above the 95% confidence level. The purple boxes in panel a, b and d are the NC and YRD regions, and the black box in panel a indicates the location of the East Asia trough.



460 **Figure 11.** Anomalies in the summer mean MDA8 in 2015 (a), 2016 (b), 2017 (c) and 2018(d), relative to the mean during 2015–2018. The black crosses and dots indicate the locations of the observation sites while the black crosses also indicate that the maximum MDA8 was larger than $265 \mu\text{g}/\text{m}^3$.

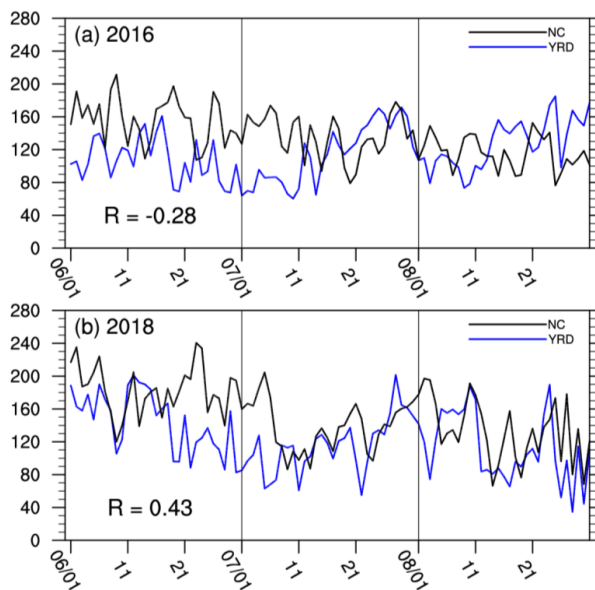
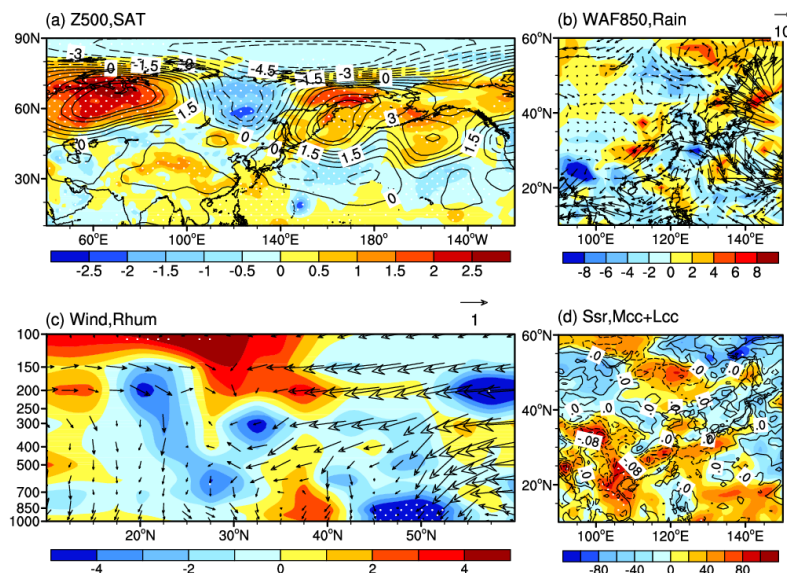


Figure 12. Variations in the MDA8 of NC (black) and the YRD (blue) in 2016 (a) and 2018 (b).



465 **Figure 13.** Anomalies of summer mean atmospheric circulations in 2016, with respect to the mean during 2015–2018.
(a) Geopotential height at 500 hPa (contours) and surface air temperature (shading), (b) water vapor flux at 850 hPa
(arrows) and precipitation (shading), (c) 100°E–120°E mean wind (arrows) and relative humidity (shading), (d)
470 downward solar radiation at the surface (shading) and the sum of low and medium cloud cover (contours). The white
dots indicate that the shading was above the 95% confidence level.

470

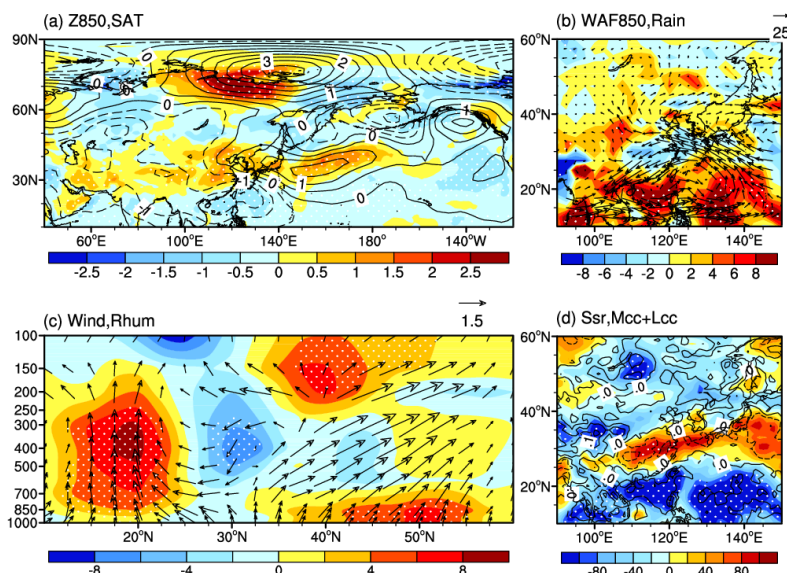


Figure 14. Anomalies of summer mean atmospheric circulations in 2018 with respect to the mean during 2015–2018.
(a) Geopotential height at 850 hPa (contours) and surface air temperature (shading), (b) water vapor flux at 850 hPa
(arrows) and precipitation (shading), (c) 100°E–120°E mean wind (arrows) and relative humidity (shading), (d)
475 downward solar radiation at the surface (shading) and the sum of low and medium cloud cover (contours). The white
dots indicate that the shading was above the 95% confidence level.